Time reversal imaging for sensor networks with optimal compensation in time

June 22, 2006

Grégoire Derveaux[1]
INRIA, Domaine de Voluceau, BP105, 78153 Le Chesnay Cedex, France

George Papanicolaou[2]
Department of Mathematics, Stanford University, CA 94305, USA

Chrysoula Tsogka[3]
Department of Mathematics, University of Chicago, IL 60637, USA

Running Title: Time Reversal Imaging for sensor networks

Submitted: June 2006 to the Journal of the Acoustical Society of America

PACS number:

43.60.Gk: Space-time signal processing, other than matched field processing

43.60.Pt: Signal processing techniques for acoustic inverse problems

43.60.Tj: Wave front reconstruction, acoustic time-reversal, and phase conjugation

---

[1] Electronic-mail: gregoire.derveaux@inria.fr
[2] Electronic-mail: papanicolaou@stanford.edu
[3] Electronic-mail: tsogka@math.uchicago.edu

Abstract

We analyze with extensive numerical simulations distributed sensor imaging algorithms for localized damage in a structure. Given a configuration of ultrasonic transducers, we assume that a full response matrix for the healthy structure is known. It is used as a basis for comparison with the response matrix that is recorded when there is damage. Our numerical simulations are done with the wave equation in two dimensions. The healthy structure is a two dimensional region containing many scatterers. We want to image point-like defects in this structure with several regularly distributed sensors. Because of the complexity of the environment, the recorded traces have a lot of delay spread and travel time migration does not work well. Instead, the traces are back propagated numerically assuming that we have knowledge of the background. Since the time at which the back propagated field will focus on the defects is unknown, we compute the Shannon entropy of the image and pick the time where it is minimal. The bounded variation norm is also a good indicator of when to stop the back propagation. This imaging method performs well for distributed sensors networks because it produces a tight image near the location of the defects at the time of refocusing. When there are several defects, the singular value decomposition of the response matrix is also carried out, at each frequency, to resolve selectively the defects.

PACS numbers: 43.60.Gk, 43.60.Pt, 43.60.Tj

I. INTRODUCTION

Signals recorded by sensors placed in a structure can be used to monitor its integrity and to detect the appearance of defects. In ultrasonic non-destructive testing the sensors are often small, isotropic transducers that operate in broadband regimes.

The regular monitoring of a structure generates huge amounts of data which are largely redundant and difficult to use. Detection can be done, in principle, by comparing the response of the structure in its normal state with that recorded when defects are present. The literature for this problem goes back some 30 years[1,2]. To what extent can these responses be used to also image the defects? Imaging the location and shape of the defects is a much more complex problem that has received a lot of attention when arrays are used[3]. Imaging with distributed sensors in structural health monitoring applications is considered in[4–7]. We consider this question in this paper using time-reversal imaging methods. Numerical back propagation of the recorded signals will focus them near the defects, which behave like weak secondary sources. However, we do not know at what time during the back propagation process this focusing will occur since the location of the defects is not known. We propose here an algorithm for optimally stopping the back propagation by using an entropy or bounded variation norm for the image. When several small defects are present we image using the singular value decomposition of the response matrix together with the optimally stopped back propagation. We carry out extensive numerical simulations in order to assess the effectiveness of this algorithm. We find that back propagation with optimal stopping works well, especially when the Green's function for the structure is known. Travel time migration imaging does not work as well because it does not use information about the background, while full wave migration in the known background is computationally very demanding and therefore not competitive.

One important difficulty for the data analysis is due to the complexity of the propagation of ultrasound in thin composite structures. Lamb waves propagating in a thin elastic structure are dispersive. Also, structures like an airplane or a bridge contain many objects like stiffeners or rivets. The propagating waves will be scattered at all these objects and the recorded signals will have long codas. In this paper, we are interested in imaging in such hetereogeneous media. We do not consider dispersive effects. Time reversal with Lamb waves for an active source problem has been investigated in[8]. Time reversal imaging with dispersive waves is an important issue that will be addressed in a later study. There are several idealizations in this approach to distributed sensor imaging that need to be pointed out. Regarding the imaging algorithm, the main one is the assumption that the wave propagation properties of the structure, its Green's function, are known. This is a reasonable one for nondestructive testing or structural health monitoring because a lot is known about the structure. Another one is the use we make of the difference of signals with and without defects, which is difficult to do in practice and requires high signal to noise ratios. Regarding the numerical simulations, they are done in two dimensions with the wave equation, without dispersion.

This paper is organized as follows. In the next section we present the numerical setup used in this study. In section III we consider the travel time migration algorithm and show that it does not perform well with the data that we use. In section IV, we present the time reversal algorithm with optimal stopping. The numerical simulations confirm the expected good performance of this algorithm as well as its reliability.

II. A DISTRIBUTED SENSOR FRAMEWORK FOR NUMERICAL SIMULATIONS

In order to assess the effectiveness of distributed sensor imaging algorithms we have carried out extensive numerical simulations with the wave equation in two dimensions. We consider the structure shown in Fig. 1. It is a domain of size 50λ by 50λ, where $\lambda = 1$ cm is the central wavelength of the probing pulse used by the sensors. All dimensions in this paper are given in units of λ. The wave speed is taken to be $c_0 = 5000\text{m.s}^{-1}$, which is typically the speed of the lowest symmetric propagating Lamb mode in a 1mm thick aluminum plate. On this plate structure we place a fixed object of size 3λ and 25 smaller objects of size $\lambda/2$ which are on the same line. The later could represent a line of rivets, for example. We simulate propagation in an infinite plate, as if we were considering a small part of a bigger structure. Reflections from boundaries provide more information at the sensors and make time reversal imaging more robust, as explained in section IV. Imaging in an infinite region is therefore an important case to consider in some detail. There is no intrinsic absorption in the structure, so the only cause of dissipation is the outgoing radiation.

The defects we want to image are two identical point-like objects, located on the plate at

(12,17) and (9,18). They are thus approximately 3λ apart. All the features and the defects in our computations are perfect reflectors with Dirichlet boundary conditions. They could also be penetrable objects, that is, heterogeneities of the background with finite propagation speed. With point-like defects this does not affect much the imaging algorithms.

The structure is illuminated with a small number of sensors regularly distributed. There are $N = 12$ of them that are placed in 4 rows of 3 sensors each. The rows of sensors are separated by 10λ and in each row the sensors are 20λ apart. The location of the sensors is denoted x_p, $1 \le p \le N$. They are point-like and isotropic, and capable of both emitting a pulse into the medium and recording the vibration at their location. The probing pulse that we use in the computations is the second derivative of a Gaussian given by

$$f(t) = (2[\alpha(t - t_0)]^2 - 1) \exp(-[\alpha(t - t_0)]^2) \tag{1}$$

where $\alpha = \pi\nu$, and t_0 is a translation of the time origin. It is shown in Fig. 3 along with its Fourier transform. Its central frequency is $\nu = 500$ kHz and with background velocity $c_0 = 5000\mathrm{m.s}^{-1}$ the central wavelength is $\lambda = 1\mathrm{cm}$. The frequency band at -6dB is approximately [220 kHz, 850kHz], which gives an 130% relative bandwidth.

The wave equation in two dimensions is solved with a numerical method based on the discretization of the mixed velocity-pressure formulation for acoustics. For the spatial discretization we use a finite element method which is compatible with mass-lumping[9,10], that is, which leads to a diagonal mass matrix so that explicit time discretization schemes can be used. For the time discretization we use an explicit second order centered finite difference scheme. In the simulations the point-like defects are modeled by small squares whose side is given by the space step of the grid, namely $\lambda/32$. The infinite medium is simulated by embedding the computational domain into a perfectly matched absorbing layer[11].

For the given distribution of sensors, the response matrix of the healthy structure is computed in the time domain. Each sensor $p = 1 \ldots N$ emits a pulse into the structure and the echoes are measured at all sensors $q = 1 \ldots N$. This response matrix is denoted $P^0(t) = (P^0_{pq}(t))_{p,q=1\ldots N}$. We call it the baseline. It is symmetric because of reciprocity. Each column of P^0 corresponds to a different illumination of the structure: the p^{th} column are the signals or traces measured at all sensors when sensor $\#p$ is firing. The response matrix of the damaged structure is computed with the same configuration of sensors and is denoted by $P^d(t)$. The difference between the damaged and healthy response matrices is denoted by $P_{pq}(t) = P^d_{pq}(t) - P^0_{pq}(t), p, q = 1 \dots N$. Henceforth we call $P(t)$ the *response matrix* (of the damaged structure). In this difference matrix the direct arrivals of emitted pulses and reflections coming from the scatterers in the healthy structure have been removed. The matrix $P(t)$ contains therefore the back-scattered echos coming from the defects and from multiple scattering between them and also with the scatterers in the healthy structure. Since the sensors are close to each other in array imaging, the direct arrivals are in the early part of the received signals. They can therefore be removed by cutting off that part of the signal, as the region to be imaged is at some distance from the array. However, in distributed sensor imaging the direct arrivals cannot be removed by a simple cut-off. This is one reason why knowledge of the response of the baseline structure is needed when imaging with distributed sensors.

The sixth column of each of the matrices $P^0(t)$, $P^d(t)$ and $P(t)$ is shown from left to right in Fig. 2. The signals are the vibrations recorded as functions of time at one of the 12 sensors, when sensor #6 is firing. All signals shown are normalized so that their maximum is 1. The direct arrival of the probing pulse is clearly visible on the traces for the healthy structure at sensors #4 to #12, because they have a direct line of sight with sensor #6. The smaller vibrations arriving at later times are from the multiple scattering with the reflectors in the healthy structure. The sensors #1 to #4 are located behind the line of rivets so there is no line of sight with sensor #6. Therefore there is no clear direct arrival of the probing pulse but rather a long coda that comes from the multiple reflections with the rivets. This signal coda is called the delay spread. The differences between $P^0(t)$ and $P^d(t)$ can hardly be seen by looking at them separately because the reflections coming from the defects are very small compared to the direct arrivals. The amplitude of the signals coming from the defects (in $P(t)$) is approximately 100 times smaller than that of the direct arrivals (in $P^0(t)$ and $P^d(t)$). The difference traces contain signals coming only from the defects and it is quite clear that the direct arrivals have been removed. However, there is also no clear arrival time coming from the defects. This is because the healthy structure around the defects has other scatterers that generate delay spread, which depends significantly on the illumination. We also note that with distributed sensors the trace peaks do not form hyperbolas as is in array imaging. It is therefore not possible to get a rough estimate of the location of the defects from a quick glance at the data, as is often the case in array imaging.

We assume that the signal to noise ratio here is very high. Therefore the presence of defects can be detected if at least one singular value of the Fourier transform of $P(t)$ is above some threshold. Our purpose is to go well beyond this step, to an algorithm that images the defects.

III. TRAVEL TIME IMAGING

Perhaps the simplest way to image with distributed sensors is by triangulation. The main difficulty in implementing triangulation is getting a reliable estimate of arrival times from the traces of the response matrix $P(t)$. This difficulty can arise from the dispersive nature of Lamb waves, as it is discussed in[7], or from multiple scattering that generates large delay spread in the traces, as described in the previous section.

Travel time imaging, or travel time migration, or Kirchhoff migration is an important imaging algorithm that is based on travel time computations. It is different from basic triangulation because it does not require the estimation of arrival times from the traces. It is used extensively in seismic array imaging[3,12] and elsewhere. Several variants of it have also been used in structural health monitoring[4–6]. The main idea in travel time migration is to compute the value of an imaging functional of the data at each "search point" y^S in the region that we want to image. With the traces recorded at the N receivers at $(x_q)_{1\leq q\leq N}$ when the sensor at x_p is firing, we compute for each y^S

$$I_p^{KM}(y^S) = \sum_{q=1}^{N} P_{pq}(\tau_p(y^S) + \tau_q(y^S)). \tag{2}$$

where $\tau_p(y^S) = |x_p - y^S|/c_0$ is the travel time from x_p to y^S and c_0 is the background propagation speed. That this is an imaging algorithm can be seen as follows. The travel time $\tau_p(y^S) + \tau_q(y^S)$ is the time for the wave to go from the source at x_p to the search point y^S and then from y^S to the receiver at x_q. If y^S is near a defect location then the trace $P_{pq}(t)$ will have a peak at that time. The imaging functional $I_p^{KM}(y^S)$ sums coherently these peak values for the different sources and receivers, producing a local maximum or minimum. However, if y^S is far from the location of a defect, then the traces will be added incoherently and $|I_p^{KM}(y^S)|$ will be small.

The imaging functional $I_p^{KM}(y^S)$ is an approximation to the least squares solution of the linearized inverse scattering problem[3,12], and its resolution gets better as the number of sensors increases. The resolution theory for travel time migration is well understood for sensor arrays in a homogeneous or smooth background[3,13,14]. It is well known, for example, that the range resolution, that is, the resolution in the direction orthogonal to the array, is controlled by the bandwidth B of the probing pulse and is given by c_0/B. The cross range resolution, that is, the resolution in the direction parallel to the array, is limited by the aperture of the array a and the distance L between the array and the defect, and it is given by $\lambda L/a$, where λ is the central wavelength. There does not appear to be a resolution theory for travel time migration with distributed sensors while range and cross range are no longer relevant terms. It is expected that the resolution is limited by the bandwidth of the probing pulse and by the uniformity of distribution of the sensors around the defect. Imaging with travel time migration improves, in general, if a large number of sensors is used.

The three images obtained with the travel time migration algorithm in our numerical simulations are shown in Fig. 4, when the structure is illuminated with the second row of sensors, that is, when sensors #2, #6 and #10 are probing. The migration images obtained with the other rows are very similar.

All images in the figures in this paper show the imaging function in a square of size 10λ centered on the defect located at (12, 17), with a grid resolution of $\lambda/4$. This imaging square is shown with dashed lines in Fig. 1. The second defect is in the upper left part of this image domain.

Because the sensor data in our simulations has a lot of delay spread, travel time migration does not work well. The three images in Fig. 4 differ a lot and depend sensitively on which sensor is illuminating. It is not possible to rely on any particular illumination more than another.

The difference traces have a lot of delay spread because of multiple scattering between the defects and the reflectors that are in the background. In travel time migration the background is assumed to be homogeneous and multiple reflexions between the defects are neglected, which is the Born approximation.

We will next introduce an imaging method that uses knowledge of the background. It gives more reliable results that are stable when different sensors illuminate.

IV. TIME REVERSAL WITH OPTIMAL STOPPING

A. Physical time reversal

In physical time reversal sensor arrays focus energy on sources with resolution that improves when there is multiple scattering[15–19]. The signal emitted by a source is received by the sensor array, it is time reversed and then re-emitted into the medium. The waves propagate back toward the source and focus around it. The refocusing location is not known in this process but the time of refocusing is known if we know at what time the source started to emit. Refocusing occurs both in space and time[15]. The spatial resolution of the focusing is better when there is a lot of multiple scattering[19,20] because the complex medium effectively enhances the size of the sensor array, and the quality and stability of the refocusing improves when the bandwidth of the pulse emitted by the source is large. Physical time reversal provides therefore an efficient way to focus energy on a defect[16] or for communications[17,21].

B. Numerical time reversal for imaging

Time reversal can also be used for imaging sources. In this case, the traces recorded at the sensors are back propagated *numerically* in an idealized medium, since the actual medium is not known in detail, in general. An image of the location of the sources is obtained by taking a snapshot of the back propagated field at the refocusing time. This procedure can be applied both with active sources and with passive scatterers. Indeed, back-propagation of the recorded traces with travel times is the migration algorithm of the previous section.

In structural health monitoring it is reasonable to assume that we have some knowledge of the healthy structure, up to some level of detail. We will assume here that the background is known, meaning that the traces can be back propagated in the healthy structure shown in Fig. 1.

For each illumination of the structure the difference traces recorded at each sensor are time reversed and back propagated numerically in the medium. Let $u_p(y,t)$ denote the field at time t and point y that is back-propagated when the traces of the p^{th} column of the response matrix P are used. Then $u_p(y,t)$ is the solution of the partial differential equation

$$\begin{cases} \dfrac{\partial^2 u_p}{\partial t^2}(y,t) - c_0^2 \Delta u_p(y,t) = \displaystyle\sum_{q=1}^{N} \delta_{(y=x_q)} P_{pq}(T-t) & \text{in } \mathbb{R}^2 \setminus \Omega, \\ u_p(y,t) = 0, & \text{on } \delta\Omega, \end{cases} \tag{3}$$

where Ω is the set of all reflectors in the healthy structure, as shown in Fig. 1, and $\delta\Omega$ denotes their boundary. Here $\delta(y = x_q)$ is the Dirac function at x_q and $(0,T)$ is the recording time interval. This equation is solved numerically with the finite element method discussed in section II.

We want to obtain an image of the defects by taking a snapshot of the back propagated field $u_p(y,t)$ at the time it refocuses on them. The problem with this approach is that the refocusing time is *not known*, as explained schematically in Fig. 5. This is a major difference between active source imaging by time reversal and the echo mode imaging. In echo mode the wave emitted by the probing sensor must first reach the defects before they can act as a secondary sources. Since the location of the defects is not known, the time t^* at which they start emitting is not known. The back-propagated field will first focus on some defect at time t^*. If we continue back propagating it will focus on the emitting sensor, which is the actual source, at time 0, but we are obviously not interested in this. Therefore we must consider ways to determine the refocusing time t^*.

We want to distinguish between back propagated fields that are spread out from those that are more focused. A simple way to do this is to pick the time at which the amplitude of the field is maximal because at that time the signals coming from all the sensors are superposed constructively. This does not work because of the decrease in amplitude with distance from the emitting source. It is not possible to compensate for this when the sensors are distributed because the defect might be anywhere, near or far from any sensor. The situation here is different from that encountered with arrays. If the defect is far enough from the array then the sensor-to-defect distance is approximately the same for all sensors and an amplitude correction could be considered.

For distributed sensors that are more or less uniformly distributed around the defects, the back propagated field is coming toward them from every direction. It will focus locally in time and it is spread around the defects both before and after the refocusing time. A way to characterize focused images is to measure them with norms that are small in that case and large otherwise. Norms that penalize images with a lot of fluctuations, a lot of speckles or many geometrical features, are called *sparsity norms.* They do not work so well with back propagation from an array because the field is coming mostly from one direction. It works well with distributed sensors as can be seen in Fig. 6.

We consider here two sparsity norms:

- The Shannon entropy, $S(u_p(.,t))$, which is a measure of the information needed to encode a pixelized image,
- The Bounded Variation norm, $BV(u_p(.,t))$, which is an L^1 sparsity norm that tends to penalize images that have a lot fluctuations.

Let $u_{ij}(t), i,j = 1 \ldots N_d$ denote the space-discretized version of the continuous field $u_p(y,t)$ at time t on a square grid with spatial step h containing N_d points in each direction. We denote by $y_{ij} = y_0 + ih\boldsymbol{e_x} + jh\boldsymbol{e_y},\ i,j = 1 \ldots N$, the discretization points, where y_0 denotes the lower left corner of this square grid and $(\boldsymbol{e_x}, \boldsymbol{e_y})$ are the coordinate vectors. We define $u_{ij}(t) = u_p(y_{ij},t), \quad i,j = 1 \ldots N_d$. In the images shown in this paper, the square grid contains 41 points in each direction and the space step is $\lambda/4$. We use a square grid for simplicity.

1. Shannon entropy

Shannon's definition[22] of the entropy of a pixelized image u_{ij} is a measure of the sparsity of the histogram of the gray levels of the image. For a given number of gray levels N_c we introduce a linear gray level scale $(c_k), k = 0 \ldots N_c$, ranging from the minimum of u_{ij} to its maximum. The histogram of gray levels of the image is defined by counting the number of pixels contained in each gray level set:

$$h_k = \sum_{i,j} \mathbf{1}_{\{[c_k, c_{k+1}]\}}(u_{ij}),\ k = 0 \ldots N_c - 1. \tag{4}$$

Here $\mathbf{1}_A$ is the characteristic function of a set A. Clearly, $\sum\limits_{k=0}^{N_c} h_k = N_d^2$ and thus (h_k/N_d^2) is the probability distribution of gray levels of the image for a given number N_c. The Shannon entropy of the image is the Boltzmann entropy of that probability distribution, defined by:

$$S(u_{ij}) = -\sum_{k=0}^{N_c-1} \left(\frac{h_k}{N_d^2}\right) \log_2 \left(\frac{h_k}{N_d^2}\right) \tag{5}$$

In this paper the number of gray levels is $N_c = 256$. The results are not sensitive to N_c unless it is very small, such as $N_c = 2$.

The entropy quantifies the amount of information needed to encode an image and is often given in bits per pixel (*bpp*). It is used in image compression[23] and for other applications in image analysis[24,25]. It penalizes back propagated fields that have a lot of speckles. The definition of entropy in Eq. (5) treats all points in the image independently. Therefore the entropy of an image whose pixels have been shuffled around has exactly the same entropy as the original.

2. *BV norm*

The bounded variation norm[26] of a regular function $u(x)$ defined in a domain Ω is given by

$$BV(u) = \int_\Omega (|u(x)| + |\nabla u(x)|)dx. \tag{6}$$

For a pixelized image u_{ij} defined on a grid with spatial step h the BV norm is given by

$$BV(u_{ij}) = h^2 \sum_{i,j} \left(|\tilde{u}_{ij}| + |\nabla_h \tilde{u}_{ij}|\right), \tag{7}$$

where $|\nabla_h \tilde{u}_{ij}|$ is a finite difference approximation of the gradient of $\tilde{u}_{ij}$. We let $\tilde{u_{ij}} = u_{ij}/\max_{i,j}(|u_{ij}|)$ be the normalized version of the image u_{ij}. As already noted above, the amplitude of the field at the time of refocusing depends on the distance between the defect and the sensors. So it is necessary to normalize the image before taking its BV norm so as to avoid dependence on field amplitudes. Note that this normalization is intrinsically made with entropy since $S(u_{ij}) = S(\alpha u_{ij})$ for all $\alpha > 0$. The BV norm penalizes images that have a lot of oscillations, because it has the gradient in it. It also penalizes images that are spread out diffusely, and the L^1 norm plays an important role in this. The BV norm is used widely in image denoising because it preserves sharp features[27,28].

3. *Time reversal imaging with optimal stopping*

The imaging algorithm we use is the following:

1. For the p^{th} column of the response matrix P, compute numerically the wave field $u_p(y,t)$ defined by Eq. (3).

2. Compute the sparsity norm (Shannon entropy or BV norm) of the field $u_{ij}(t) = u_p(y_{ij}, t)$ in the imaging domain (y_{ij}) as a function of time.
3. Pick the time at which it is minimal, denote it t^*.
4. Plot the image $u_{ij}(t^*)$.

4. Results of numerical simulations

The entropy and BV norm versus time are plotted in Fig. 6 for the three illuminations from the second row of sensors (sensors #2, #6 and #10). The back propagated wave fields are also shown at the optimal time. These three illuminations are typical and the results obtained with the other rows of sensors are similar. The time plots are shown in a time window that is zoomed near the focusing events. The results are good because they give rather clean images of the defects. There are few speckles, the focusing spot is smooth, the defects are at the right locations, and there are no ghosts. The two norms, Shannon entropy and BV, give comparable results. They both pick a stopping time close to the refocusing time on one of the 2 defects. The optimal stopping times picked by the two norms differ by at most one or two time steps.

However, since only one refocusing time is picked with this technique, one cannot get an image for each defect at the same time. This method images the strongest defect as it is perceived by the sensors for a given illumination of the structure. For example, the method picks the defect located at (9, 18) when sensor #2 is illuminating, and there is only one minimum, which means that only one defect is detectable. This may be explained roughly by noting that the defect (9, 18) and the sensor #2 are located on the same side of the line of rivets. On the other hand, The strength of the defects is roughly the same when they are illuminated with sensors #6 or #10. There are 2 clear minima that have almost the same value, both with the entropy and the BV norm. The minima are focusing times on each of the two defects. Therefore it is not possible to select one minimum rather than the other. This is an illumination issue that is best dealt with the Singular Value Decomposition (SVD) that allows for selective imaging of each defect. It is discussed in the next section.

C. Separation of the defects by Singular Value Decomposition

1. SVD of the Response Matrix in the frequency domain

The relation between the singular vectors of the the response matrix $P(t)$ and the scatterers has been analyzed extensively[29–31]. Each localized defect can be associated with a singular vector of the response matrix, except for a few degenerate cases. It is called the DORT method, which is the French acronym for "Decomposition of the Time Reversal Operator". The SVD is a way of finding the optimal illumination of a defect[32,33], that is, the one that generates the strongest received signals at the sensors. Selective time reversal focusing using the SVD of the response matrix has been successfully used theoretically and experimentally[29–31], as well as for imaging in random media[34,35].

One rather direct application of the SVD of the response matrix is estimating the number of localized defects[15]. The number of non-zero, leading singular values is an estimate of the number of localized defects. This is seen very well in our numerical simulations. The first three singular values versus frequency are shown in Fig. 7. There are clearly 2 distinct leading eigenvalues at each frequency inside the bandwidth of the probing pulse, which correspond to the two point-like defects. These two singular values are very well separated over the frequency band. This could not have been anticipated since the defects are identical. The curves of singular values versus frequency will, in general, cross each other.

Localized defects are said to be well resolved (or well separated) if the illuminating vectors associated with them are orthogonal. The elements of the illuminating vectors are the Green's functions from the sensors to the defects[35]. These vectors are also right singular vectors in this case. Of course a larger number of sensors helps in resolving defects so illuminating vectors are more likely to be orthogonal in that case. We consider imaging with time reversal and the SVD in the next section.

2. Imaging the defects using the traces projected on each singular vector

We can say that, *in principle*, the Singular Value Decomposition transforms an echo mode problem into an active source problem. This is because at least for well separated defects the singular vectors are also illuminating vectors to the unknown defect locations. However, because they carry an arbitrary, frequency-dependent phase, the singular vectors look *incoherent* in the time domain. In order to get rid of this arbitrary phase, we first project the response matrix on the space spanned by each singular vector. We now image the defects with the response matrix $P_k(t), k = 1 \ldots M$, obtained by projection of the full response matrix onto each leading singular vector[35]. The p^{th} column of the Fourier transform of $P_k(t)$ is given by

$$\hat{P}_k^{(p)}(\omega) = \left(\hat{U}_k^H(\omega)\, \hat{P}^{(p)}(\omega)\right) \hat{U}_k(\omega), \qquad p = 1, \ldots N. \tag{8}$$

Here $\hat{P}^{(p)}(\omega)$ denotes the p^{th} column of Fourier transform of the full response matrix $\hat{P}(\omega)$. Because of the orthogonality of the singular vectors, this projection removes the reflections coming from the other defects. We can think of $P_k(t)$ as the response matrix of the distributed sensors when only the k^{th} localized defect is present.

Since the phases of the projected response matrices are preserved, any algorithm that can be used for processing the original response matrix $P(t)$ can also be used with the projected matrices, without any change. For example, this can be done with travel time migration or with time reversal imaging and optimal stopping. By analogy with the columns of $P(t)$, we refer to the columns of $P_k(t)$ as responses from illumination by the sensor labeled with the column index.

Time reversal images obtained by optimal stopping using the traces projected on the first and second singular vectors are shown in Fig. 8 and Fig. 9, respectively. As before, only results obtained with the illuminations corresponding to the second row of sensors (#2, #6 and #10) are shown, for they are typical. The BV norm and entropy versus time are plotted above each image.

First, it clear that all the images obtained with the first singular vector focus on the defect at (9, 18) and all those obtained with the second singular vector focus on the other defect. This illustrates well the stability of this algorithm. For the images obtained with data projected on the first singular vector there is now only one minimum for all 12 illuminations. So the ambiguity that was noted in the previous section has disappeared. This remark holds also for images obtained with the data projected on the second singular vector. Moreover, in this case the illumination of the defect at (12, 17) from sensor #2 is now possible. This is an illustration of the ability of the Singular Value Decomposition to provide an optimal illumination that will focus selectively on one particular localized defect.

D. Cumulative images

All the algorithms presented above give an image for each illumination of the medium. The images can be enhanced by averaging over all illuminations. More precisely, if $I_p(y^S)$ denotes the image with the p^{th} column of the response matrix with either travel time migration, time reversal imaging with entropy stopping or time reversal imaging with BV stopping, we form the following cumulative image:

$$I(y^S) = \frac{1}{N} \sum_{p=1}^{N} \frac{I_p(y^S)}{\max\limits_{y^S} |I_p(y^S)|} \tag{9}$$

Note that forming the mean value is one possibility among many.

We have computed cumulative images obtained with the traces of the original response matrix as well as with the traces projected on the first and second singular vectors. Results are shown in Fig. 10. Note that the averages shown are computed with all illuminations and not only the three illuminations that were shown previously. As expected, these images have fewer speckles. They show that even with averaging, the travel time migration algorithm does not perform well. Projection on the singular vectors does not improve the performance of this algorithm.

The time reversal algorithm takes advantage of the multiple scattering and of knowledge of the Green's function of the healthy structure so it works well with both entropy stopping and BV stopping. When used with the original traces the defects are imaged as if they have different strength, depending on how they are perceived by the distributed sensors. The projection onto the singular vectors of the response matrix improves the resolution of the defects.

V. IMAGING OF AN EXTENDED DEFECT

a. Formulation of the problem We consider now the imaging of a spatially extended defect, rather than two point-like defects. The defect has the shape of a cross as shown in Fig. 11. Each of the four sides of the cross is of size λ times $\lambda/2$, so that its overall size is 2.5λ. Its shape is not convex, which makes it more difficult to image. Its size has been chosen to be larger that the resolution limit so that it may be possible to image its different features. As in the previous computations, the defect is modeled as a perfect reflector using

Dirichlet boundary conditions. The healthy structure is the one shown in Fig. 1. Both the response matrix of the healthy and of the damaged structure are computed. We want to image the shape of the defect using the difference traces.

b. Travel time migration The results obtained using travel time migration are shown in Fig. 13 for three different illuminations of the medium (the second row of sensors, #2, #6 and #10). As in the case of two point-like defects, the results are very unstable with respect to the illumination. This is due to the multiple scattering between the defects and the scatterers that are present in the healthy structure, which is not taken into account in travel time migration.

c. Singular Value Decomposition In the case of an extended defect the number of leading singular values is not related to it in a simple manner[36–38]. The 12 singular values of the response matrix are plotted as functions of frequency in Fig. 12.

d. Time-Reversal algorithm The images obtained with the time reversal algorithm described in section IV for three different illuminations of the structure (#2, #6 and #10) are shown in Fig. 14. For simplicity, only the results obtained using the BV norm are shown. The images we get using the entropy stopping are similar. Even for an extended defect, this algorithm gives an image of one part of the object, the one that has the strongest reflection, depending on the illumination. However, it gives an image of the back propagated field at only one time. Therefore we cannot expect to get an image of the defect with only one illumination because the back propagated field does not surround it at one particular time. If the illumination is coming from the left of the defect, then the image tends show the left tip of the cross, as can be seen in the left image in Fig. 14. If the illumination is coming from the right, then the right tip of the cross can be seen in the right image in Fig. 14.

A rough overall image of the damage can be obtained by summing over the images with different illumination, as in Eq. (9). The cumulative images obtained for the three algorithms (travel time migration, time reversal with entropy stop and time reversal with BV stop) are shown at the top of Fig. 15. The image obtained by simple summation over each illumination shows only the strongest edge of the cross. The other parts of the cross do not appear because they cancel out along with the speckles. We can get around this problem if we first threshold the image obtained for each illumination and then sum over the illuminations. More precisely we compute:

$$\tilde{I}_p(y^S) = \begin{cases} I_p(y^S), & \text{if } |I_p(y^S)| \geq \alpha \max\limits_{y^S} |I_p(y^S)| \\ 0, & \text{otherwise} \end{cases} \tag{10}$$

where $\alpha \in [0,1]$ is a thresholding parameter. We then form

$$\tilde{I}(y^S) = \frac{1}{N} \sum_{p=1}^{N} \tilde{I}_p(y^S).$$

The images obtained by thresholding (with $\alpha = 0.6$) and summation are shown at the bottom of Fig. 15. The image obtained with travel time migration is definitely better than the images obtained for single illuminations. One can even guess the shape of right side of the cross. However there are still speckles and the size of the defect is overestimated. The images obtained with the time reversal algorithm are more stable and have fewer speckles. Even if they do not provide a clear contour of the defect, some important features can be seen and its size is rather well estimated.

VI. SUMMARY AND CONCLUSIONS

Imaging with distributed sensors is different from imaging with arrays mainly because we need to know the response matrix of the healthy structure in order to remove direct arrivals and other strong scattering from the background. There are many important issues that need to be addressed in order to deal effectively with noise in the data and with small scale inhomogeneities in the structure, which are not considered here.

We have presented here a detailed numerical study of several algorithms for distributed sensor imaging in the context of structural health monitoring. When the propagation characteristics of the healthy structure are known, as we assume, then time reversal imaging with optimal stopping, introduced here, gives good images of localized defects. When we also use the singular value decomposition, then the time reversal images improve. Time reversal imaging with distributed sensors also gives rough but stable images for extended defects.

Acknowledgments

The work of G. Derveaux, G. Papanicolaou and C. Tsogka was partially supported by the Office of Naval Research N00014-02-1-0088, by the National Science Foundation DMS-0354674-001 and CMS-0451213, and by DARPA/ARO 02-SC-ARO-1067-MOD 1.

[1] F. Gustafsson. *Adaptive filtering and change detection.* Wiley and Sons, 2000.

[2] M. Basseville. Lessons learned from the theory and practive of change detection. In *Proceedings of the 5th International Workshop on Structural Health Monitoring, Stanford, USA*, pages 929–936, 2005.

[3] N. Bleistein, J. K. Cohen, and Jr. J. W. Stockwell. *Mathematics of Muldimensional Seismic Imaging, Migration and Inversion.* Springer, New York, 2001.

[4] Chun H Wang, James T Rose, and Fu-Kuo Chang. A synthetic time-reversal imaging method for structural health monitoring. *Smart Materials and Structures*, 13(2):415–423, 2004.

[5] L. Wang and F. G. Yuan. Damage identification in a composite plate using prestack reverse-time migration technique. *Structural Health Monitoring*, 4(3):195–211, 2005.

[6] Jeong-Beom Ihn, Fu-Kuo Chang, Jerry Huang, and Mark Derriso. Diagnostic imaging technique for structural health monitoring. In *Proceedings of the 2nd International Workshop on Structural Health Monitoring, Stanford, USA*, 2003.

[7] Michel Lemistre and Daniel Balageas. Structural health monitoring system based on diffracted lamb wave analysis by multiresolution processing. *Smart Materials and Structures*, 10(3):504–511, 2001.

[8] Ros E. Ing and Mathias Fink. Time-reversed lamb waves. *IEEE Trans. on Ultrasonics, Ferroelectrics, and Frequency Control*, 45(4):2192–2197, 1998.

[9] E. Bécache, P. Joly, and C. Tsogka. An analysis of new mixed finite elements for the approximation of wave propagation problems. *SIAM J. Numer. Anal.*, 37(4):1053–1084 (electronic), 2000.

[10] E. Bécache, P. Joly, and C. Tsogka. Etude d'un nouvel élément finin mixte permettant la condensation de masse. *C. R. Acad. Sci. Paris Sér. I Math*, 324:1281–1286, 1997.

[11] Jean-Pierre Berenger. A perfectly matched layer for the absorption of electromagnetic waves.

J. Comput. Phys., 114(2):185–200, 1994.

[12] Jon F. Claerbout. *Imaging the earth interior.* Blackwell Scientific Publications, Palo Alto, USA, 1985.

[13] G. Beylkin and R. Burridge. Linearized inverse scattering problems in acoustics and elasticity. *Wave Motion*, 12(1):15–52, 1990.

[14] Liliana Borcea, George Papanicolaou, and Chrysoula Tsogka. Interferometric array imaging in clutter. *Inverse Problems*, 21(4):1419–1460, 2005.

[15] Mathias Fink and Claire Prada. Acoustic time-reversal mirrors. *Inverse Problems*, 17(1):R1–R38, 2001.

[16] Mathias Fink. Time reversed acoustics. *Physics Today*, 50(3):34–40, march 1997.

[17] W. A. Kuperman, William S. Hodgkiss, Hee Chun Song, T. Akal, C. Ferla, and Darrell R. Jackson. Phase conjugation in the ocean: Experimental demonstration of an acoustic time-reversal mirror. *The Journal of the Acoustical Society of America*, 103(1):25–40, 1998.

[18] D. R. Dowling and D. R. Jackson. Narrow band performance of phase conjugate arrays in dynamic random media. *J. Acoust. Soc. Am.*, 91:3257–3277, 1992.

[19] P. Blomgren, G. Papanicolaou, and H. Zhao. Super-resolution in time-reversal acoustics. *Journal of the Acoustical Society of America*, 111:238–248, 2002.

[20] A. Derode, P. Roux, and M. Fink. Robust acoustic time reversal with high-order multiple scattering. *Physical Review Letters*, 75:4206–4209, 1995.

[21] G. Montaldo, G. Lerosey, A. Derode, A. Tourin, J. de Rosny, and M. Fink. Telecommunication in a disoredered envrironment with iterative time reversal. *Waves Random Media*, 14:287–302, 2004.

[22] C. E. Shannon. A mathematical theory of communication. *Bell System Tech. J.*, 27:379–423, 1948.

[23] S. Mallat. A theory for multiresolution signal decomposition: the wavelet representation. *IEEE Trans. On Pattern Analysis and Machine Intelligence*, 11:674–693, 1989.

[24] J. Sporring and J. Weickert. Information measures in scale-spaces. *IEEE Trans. On Information Theroy*, 45:1051–1058, 1999.

[25] J. Grazzini, A. Turiel, and H. Yahia. Presegmentation of high-resolution satellite images with a multifractal reconstruction scheme based on an entropy criterium. In *IEEE International Conference on Image Processing ICIP, Genova, Italy, September, 11-14 2005.*, 2005.

[26] Tony F. Chan and Jianhong Shen. *Image processing and analysis*. Society for Industrial and Applied Mathematics (SIAM), Philadelphia, PA, 2005. Variational, PDE, wavelet, and stochastic methods.

[27] Leonid I. Rudin, Stanley Osher, and Emad Fatemi. Nonlinear total variation based noise removal algorithms. *Physica D: Nonlinear Phenomena*, 60:259–268, november 1992.

[28] Yen-Hsi Richard Tsai and Stanley Osher. Total variation and level set based methods in image science. *Acta Numerica*, 1:1–61, 2005.

[29] C. Prada and M. Fink. Eigenmodes of the time reversal operator: A solution to selective focusing in multiple-target media. *Wave Motion*, 20:151–163, 1994.

[30] Claire Prada, Sebastien Manneville, Dimitri Spoliansky, and Mathias Fink. Decomposition of the time reversal operator: Detection and selective focusing on two scatterers. *The Journal of the Acoustical Society of America*, 99(4):2067–2076, 1996.

[31] Claire Prada and Jean-Louis Thomas. Experimental subwavelength localization of scatterers by decomposition of the time reversal operator interpreted as a covariance matrix. *The Journal of the Acoustical Society of America*, 114(1):235–243, 2003.

[32] Gabriel Montaldo, Mickael Tanter, and Mathias Fink. Real time inverse filter focusing by iterative time reversal. *The Journal of the Acoustical Society of America*, 112(5):2446–2446, 2002.

[33] Margaret Cheney, David Isaacson, and Matti Lassas. Optimal acoustic measurements. *SIAM J. Appl. Math.*, 61(5):1628–1647 (electronic), 2001.

[34] James G. Berryman, Liliana Borcea, George C. Papanicolaou, and Chrysoula Tsogka. Statistically stable ultrasonic imaging in random media. *The Journal of the Acoustical Society of America*, 112(4):1509–1522, 2002.

[35] Liliana Borcea, George Papanicolaou, Chrysoula Tsogka, and James Berryman. Imaging and time reversal in random media. *Inverse Problems*, 18(5):1247–1279, 2002.

[36] Hongkai Zhao. Analysis of the response matrix for an extended target. *SIAM J. Appl. Math.*, 64(3):725–745 (electronic), 2004.

[37] David H. Chambers and A. K. Gautesen. Time reversal for a single spherical scatterer. *The Journal of the Acoustical Society of America*, 109(6):2616–2624, 2001.

[38] Songming Hou, Knut Solna, and Hongkai Zhao. Imaging of location and geometry for extended targets using the response matrix. *J. Comput. Phys.*, 199(1):317–338, 2004.

Figure captions

Fig. 1: Description of the structure. It is a plate of size 50λ by 50λ on which are placed a fixed object of size 3λ and 25 smaller objects of size $\lambda/2$. $\lambda = 1$ cm is the central wavelength of the probing pulse used by the sensors. All dimensions are given in units of λ. The wave speed is taken to be $c_0 = 5000\text{m.s}^{-1}$. For numerical simulations the domain is surrounded by Perfectly Matched Layers (PML) in order to simulate propagation in the free space. We want to image two point-like defects shown by the red dots. All images in this paper show the imaging function in a square of size 10λ centered on the defect located at (12, 17), with a grid resolution of $\lambda/4$. This imaging square is shown with dashed lines.

Fig. 2: Traces recorded at all 12 sensors when sensor # 6 is firing. ¿From left to right: Traces in the healthy structure, in the damaged structure and difference between them. All signals shown here are normalized so that their maximum is 1. X-axis: time, Y-axis: number of sensor.

Fig. 3: The probing pulse used by the sensors in the time domain (left) and its Fourier transfom (right). It is a second derivative of a Gaussian whose central frequency is 500kHz.

Fig. 4: Travel time or Kirchhoff Migration images in a square domain of size 10λ centered at $(12, 17)$. Each figure corresponds to a different illumination of the structure. ¿From left to right, illumination with sensor # 2, # 6 and # 10.

Fig. 5: Schematic of echo-mode Time Reversal explaining why the refocusing time is not known.

Fig. 6: **Top 2 rows:** Entropy versus time of the back propagated field in a square domain of size 10λ centered at $(12, 17)$ and snapshot of the back propagated field at the time where entropy is minimum. Each figure corresponds to a different illumination of the structure. ¿From left to right, illumination with sensor # 2, # 6 and # 10. **Bottom 2 rows:** Same results with BV norm.

Fig. 7: The first three singular values of the response matrix $\hat{P}(\omega)$ versus frequency. There are clearly two distincts leading singular values at each frequency in the frequency band, which correspond to the two point-like defects.

Fig. 8: Same as Fig. 6 but with back propagating traces projected on the first singular vector.

Fig. 9: Same as Fig. 6, but with back propagating traces projected on the second singular vector.

Fig. 10: Cumulative images obtained by summation over each illumination as in Eq. (9). **Left:** With full traces, **Middle:** With traces projected on the first singular vector, **Right:** With traces projected on the second singular vector.

Fig. 11: Schematic of the extended defect. Zoom in the square of size 10λ centered at the point $(12, 17)$. The defect is a cross whose 4 sides are of size λ times $\lambda/2$, so that its overal size is 2.5λ.

Fig. 12: The twelvesingular values of the response matrix $\hat{P}(\omega)$ versus frequency when the defect is the cross depicted in Fig. 11 The number of singular values of the response matrix is not related in a simple manner to the defect in the structure.

Fig. 13: Travel time or Kirchhoff Migration in a square domain of size 10λ centered at $(12, 17)$ when the damage is the cross depicted in Fig. 11. Each figure corresponds to a different illumination of the structure. ¿From left to right, illumination with sensor # 2, # 6 and # 10.

Fig. 14: BV norm versus time of the back propagated field in a square domain of size 10λ centered at $(12, 17)$ and snapshot of the back propagated field at time where BV norm is minimum. The damage is the cross presented on Fig. 11 . Each figure corresponds to a different illumination of the structure. ¿From left to right, illumination with sensor # 2, # 6 and # 10.

Fig. 15: Imaging of a the cross shaped defect depicted in Fig. 11. **Left:** Kirchhoff-Migration, **Middle:** Time-reversal imaging with entropy stopping, **Right:** Time-reversal imaging with BV stopping, **Top:** Cumulative images obtained by summation over each illumination as in Eq. (9). **Bottom:** Cumulative images after thresholding as discussed in Eq. (10).

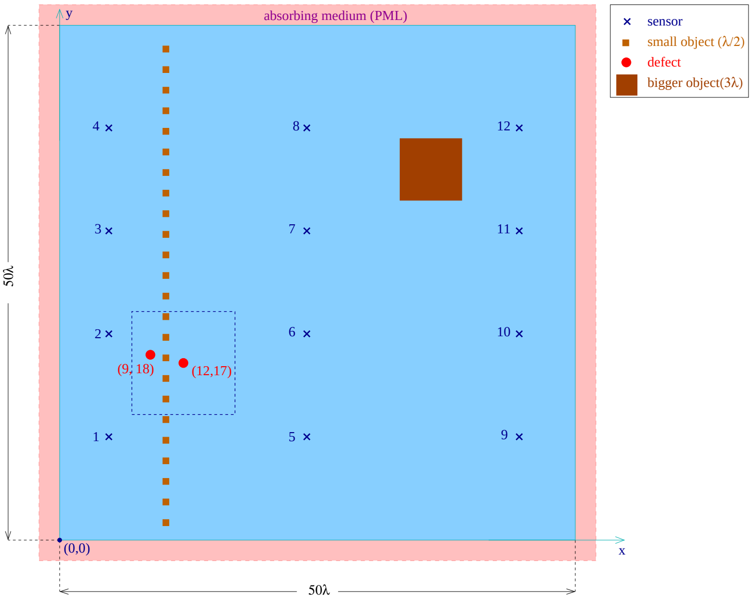

FIG. 1: Description of the structure. It is a plate of size 50λ by 50λ on which are placed a fixed object of size 3λ and 25 smaller objects of size $\lambda/2$. $\lambda = 1$ cm is the central wavelength of the probing pulse used by the sensors. All dimensions are given in units of λ. The wave speed is taken to be $c_0 = 5000\text{m.s}^{-1}$. For numerical simulations the domain is surrounded by Perfectly Matched Layers (PML) in order to simulate propagation in the free space. We want to image two point-like defects shown by the red dots. All images in this paper show the imaging function in a square of size 10λ centered on the defect located at (12, 17), with a grid resolution of $\lambda/4$. This imaging square is shown with dashed lines.

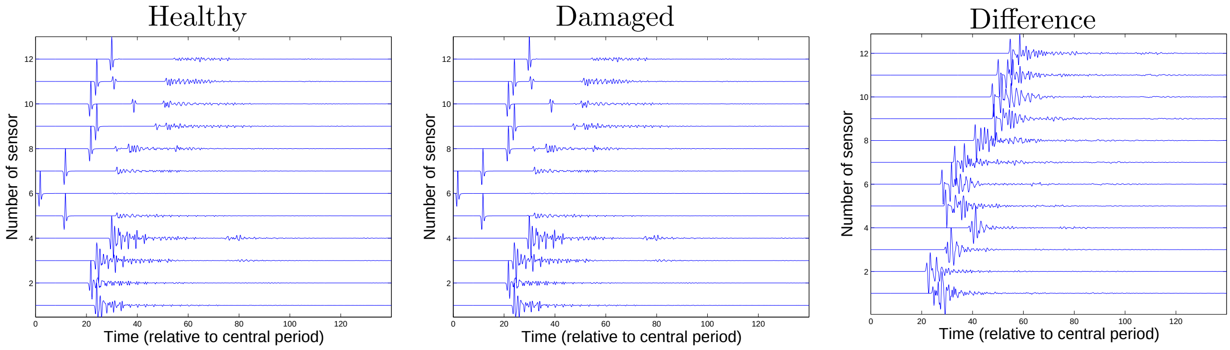

FIG. 2: Traces recorded at all 12 sensors when sensor # 6 is firing. ¿From left to right: Traces in the healthy structure, in the damaged structure and difference between them. All signals shown here are normalized so that their maximum is 1. X-axis: time, Y-axis: number of sensor.

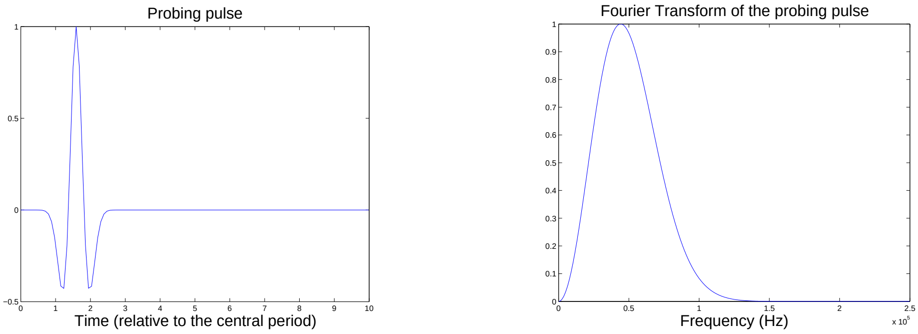

FIG. 3: The probing pulse used by the sensors in the time domain (left) and its Fourier transfom (right). It is a second derivative of a Gaussian whose central frequency is 500kHz.

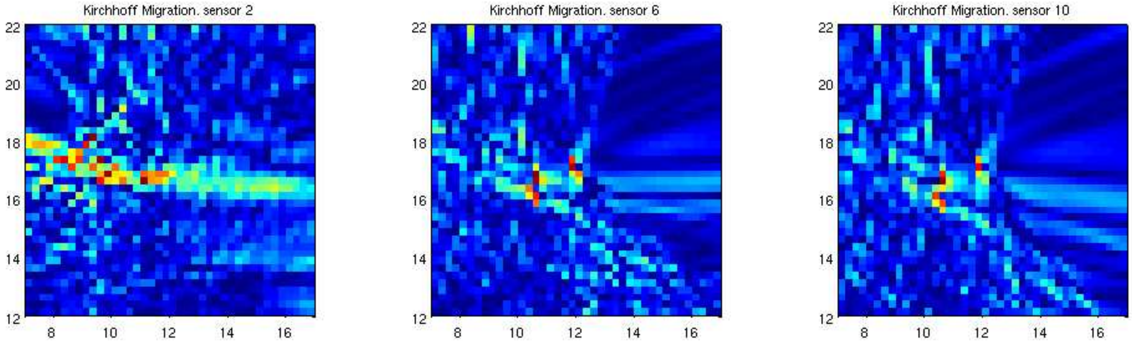

FIG. 4: Travel time or Kirchhoff Migration images in a square domain of size 10λ centered at $(12, 17)$. Each figure corresponds to a different illumination of the structure. ¿From left to right, illumination with sensor # 2, # 6 and # 10.

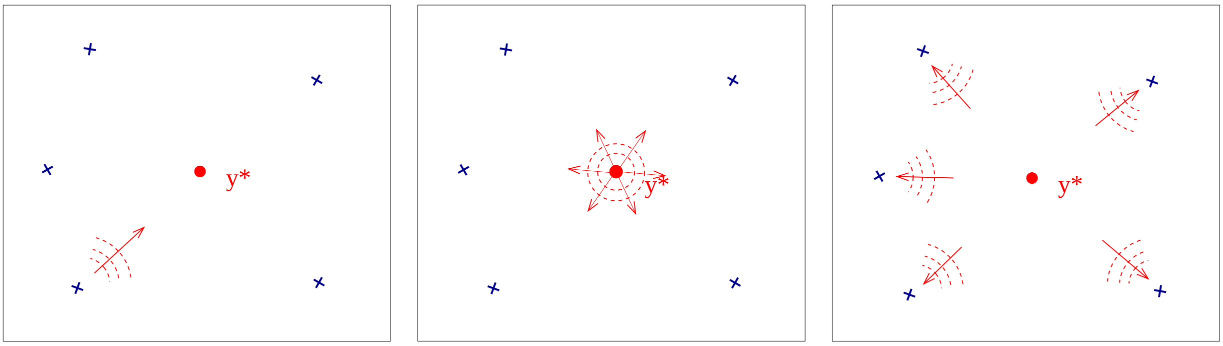
Forward propagation

Sensor p sends a pulse at time $t = 0$

Defect y^* starts emitting later on an unknown time $t = t^*$ as a secondary source

The traces are recorded at all sensors

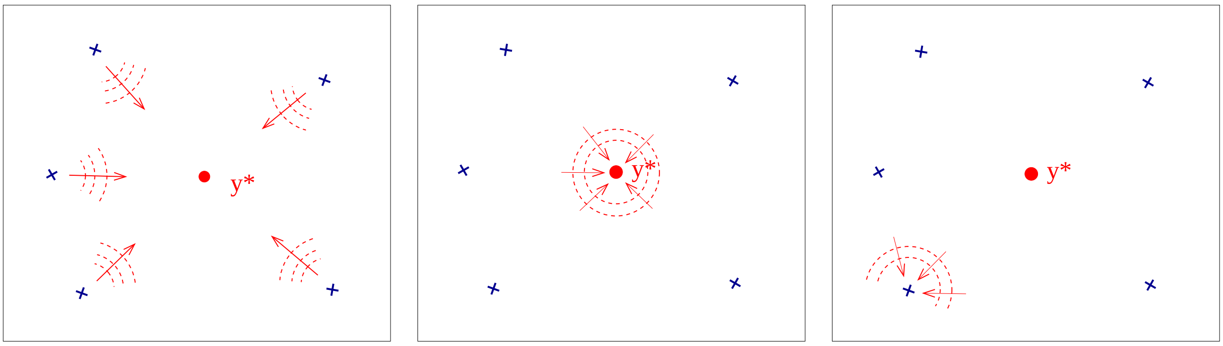
Back propagation

All sensors re-emit the time reversed traces

The back propagated field focuses first on the defect y^* at unknown time $t = t^*$

Then the back propagated field focuses on the illuminating sensor p at time $t = 0$

FIG. 5: Schematic of echo-mode Time Reversal explaining why the refocusing time is not known.

Time Reversal Imaging with entropy stopping

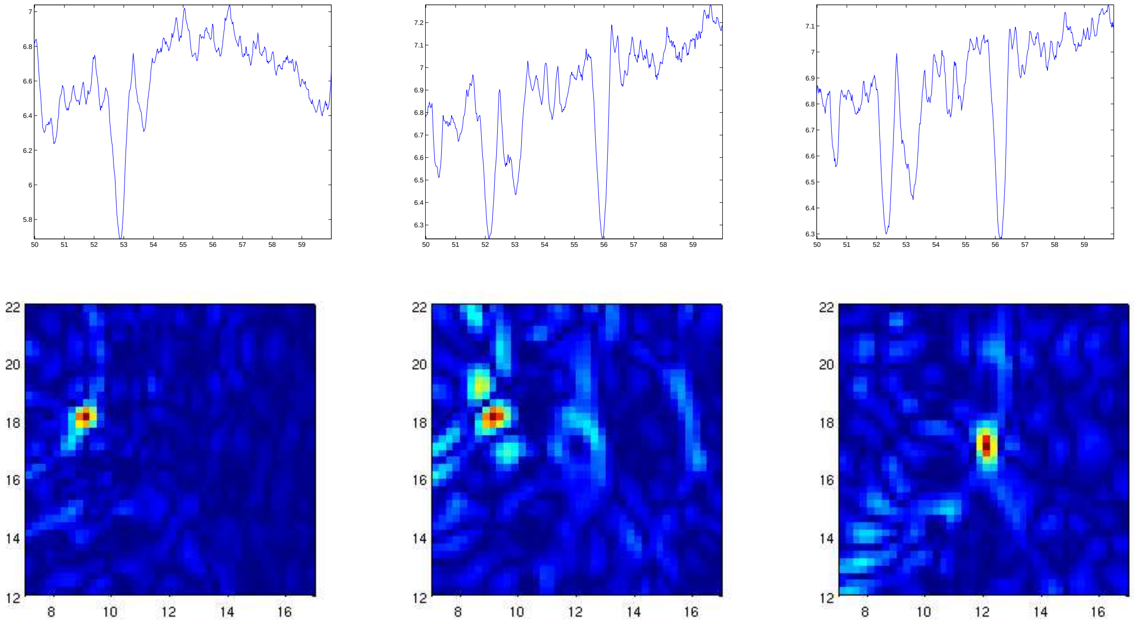

Time Reversal Imaging with BV stopping

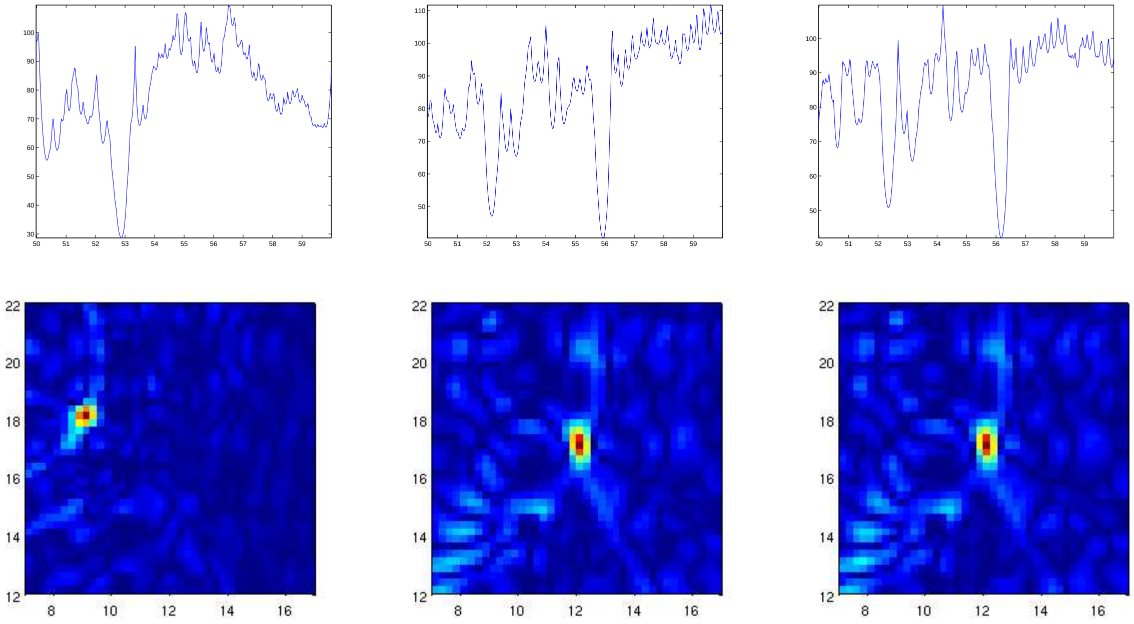

FIG. 6: **Top 2 rows:** Entropy versus time of the back propagated field in a square domain of size 10λ centered at $(12, 17)$ and snapshot of the back propagated field at the time where entropy is minimum. Each figure corresponds to a different illumination of the structure. ¿From left to right, illumination with sensor # 2, # 6 and # 10. **Bottom 2 rows:** Same results with BV norm.

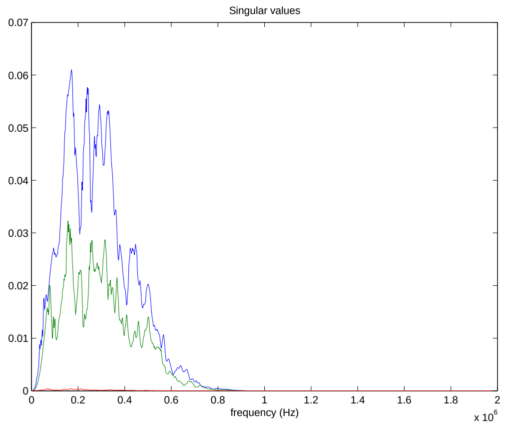

FIG. 7: The first three singular values of the response matrix $\hat{P}(\omega)$ versus frequency. There are clearly two distincts leading singular values at each frequency in the frequency band, which correspond to the two point-like defects.

Time Reversal Imaging with entropy stopping

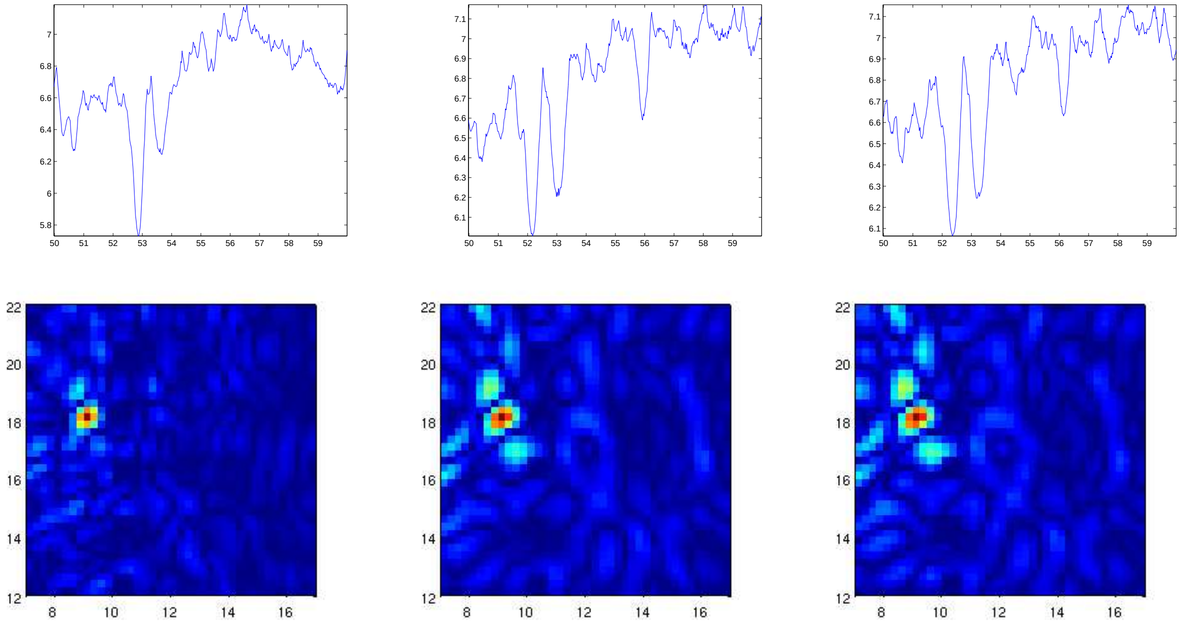

Time Reversal Imaging with BV stopping

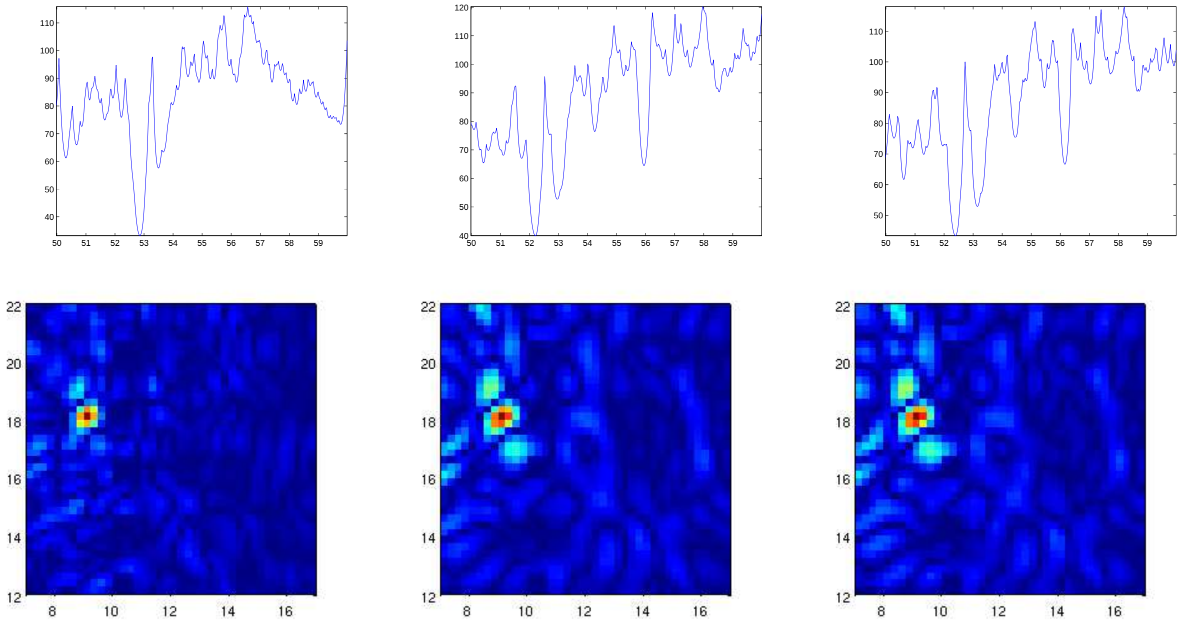

FIG. 8: Same as Fig. 6 but with back propagating traces projected on the first singular vector.

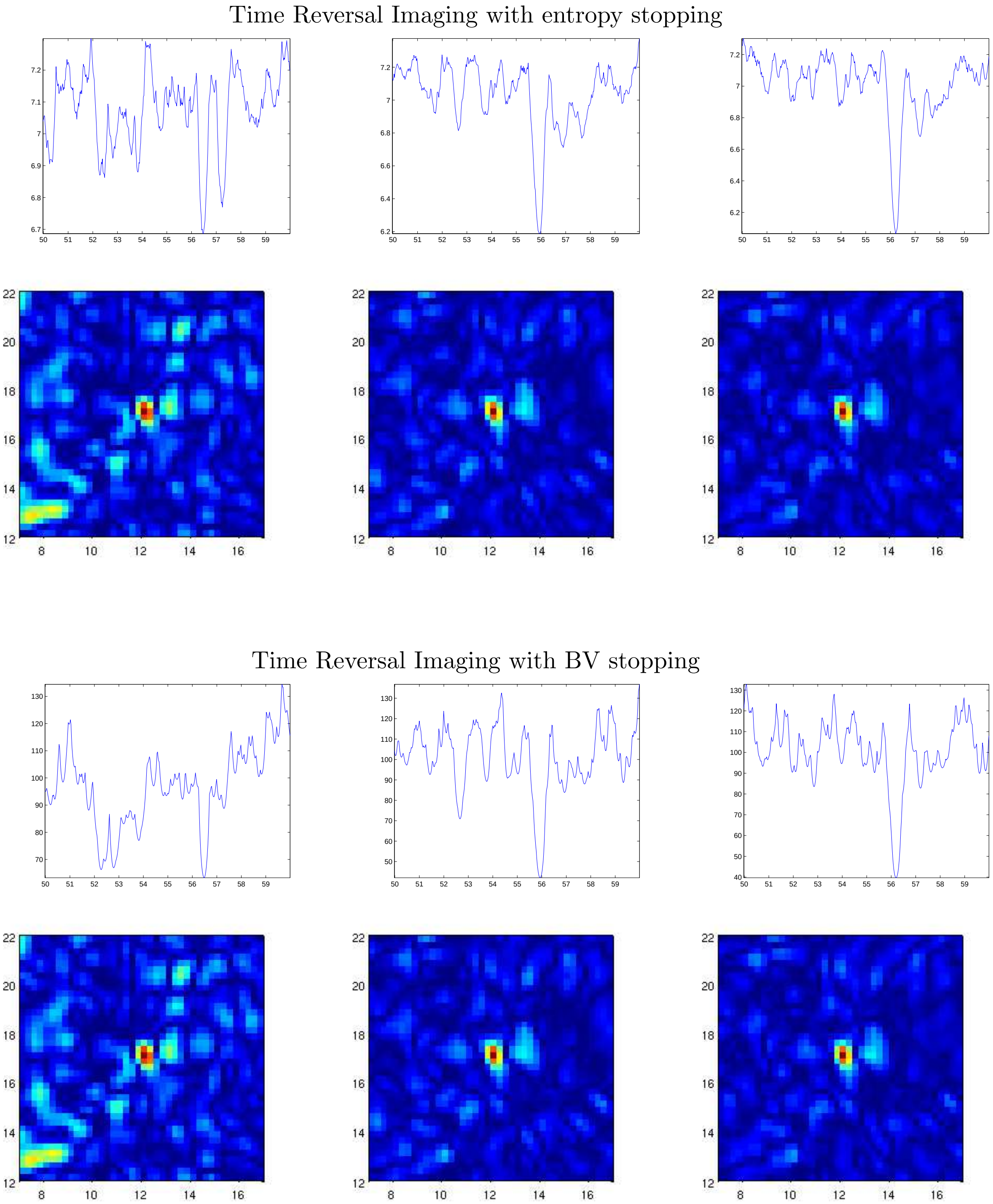

FIG. 9: Same as Fig. 6, but with back propagating traces projected on the second singular vector.

Cumulative Kirchhoff-Migration

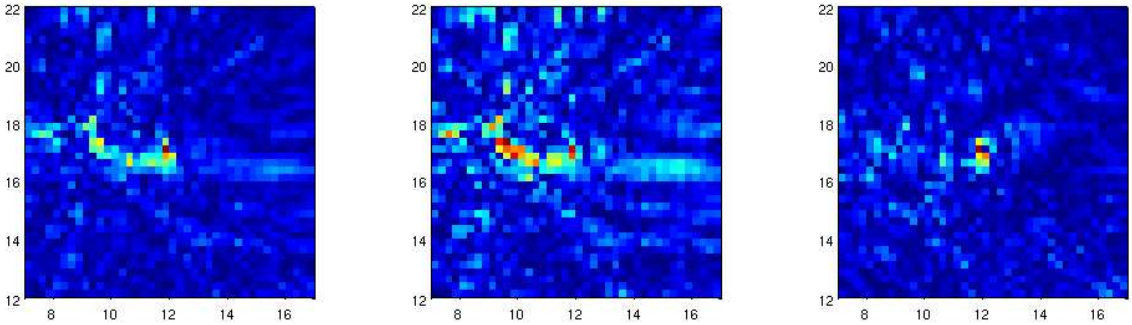

Cumulative Time Reversal Imaging with entropy stopping

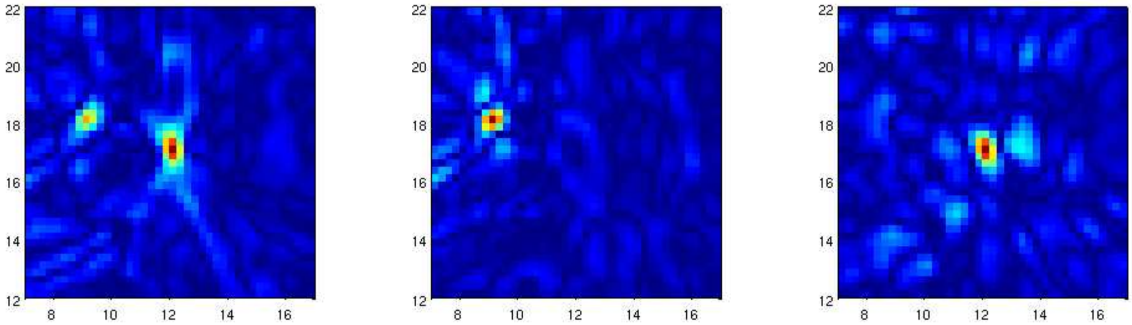

Cumulative Time Reversal Imaging with BV stopping

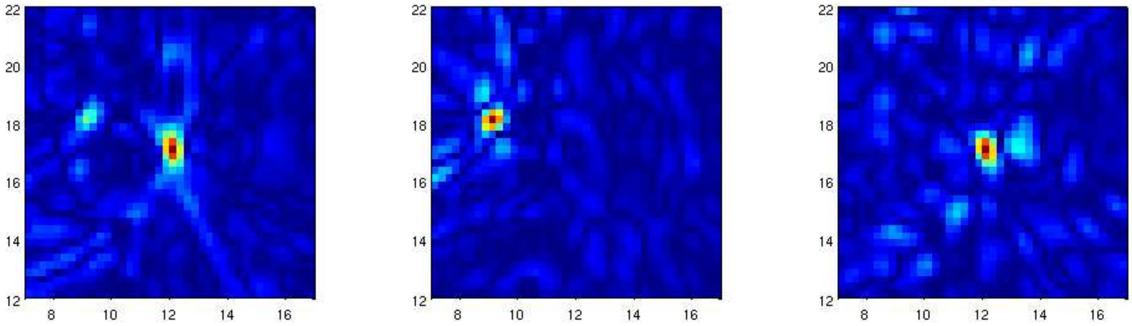

FIG. 10: Cumulative images obtained by summation over each illumination as in Eq. (9). **Left:** With full traces, **Middle:** With traces projected on the first singular vector, **Right:** With traces projected on the second singular vector.

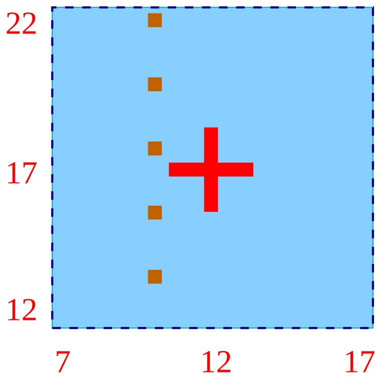

FIG. 11: Schematic of the extended defect. Zoom in the square of size 10λ centered at the point $(12, 17)$. The defect is a cross whose 4 sides are of size λ times $\lambda/2$, so that its overal size is 2.5λ.

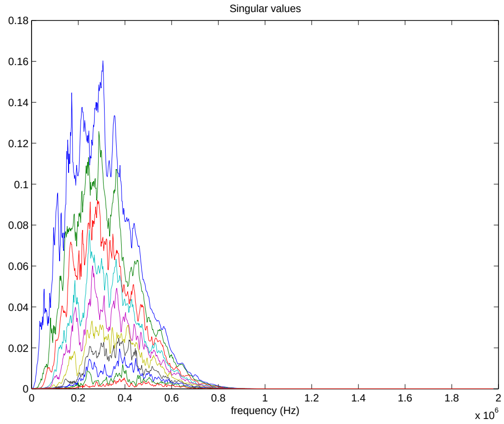

FIG. 12: The twelvesingular values of the response matrix $\hat{P}(\omega)$ versus frequency when the defect is the cross depicted in Fig. 11 The number of singular values of the response matrix is not related in a simple manner to the defect in the structure.

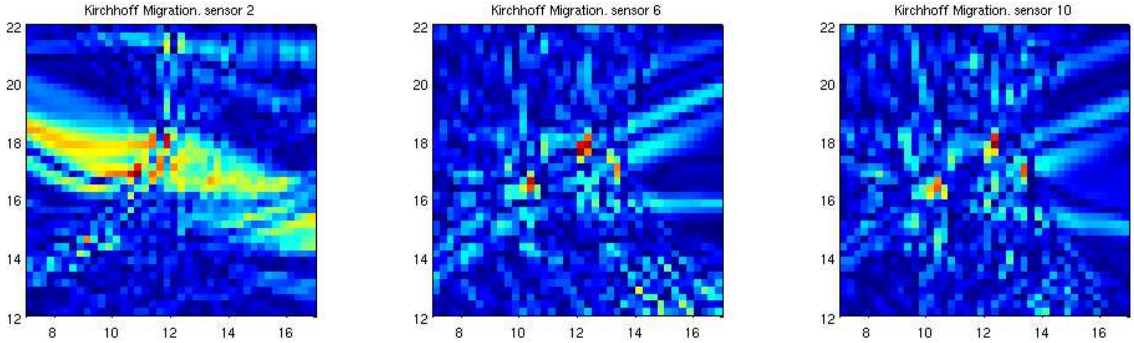

FIG. 13: Travel time or Kirchhoff Migration in a square domain of size 10λ centered at $(12, 17)$ when the damage is the cross depicted in Fig. 11. Each figure corresponds to a different illumination of the structure. ¿From left to right, illumination with sensor # 2, # 6 and # 10.

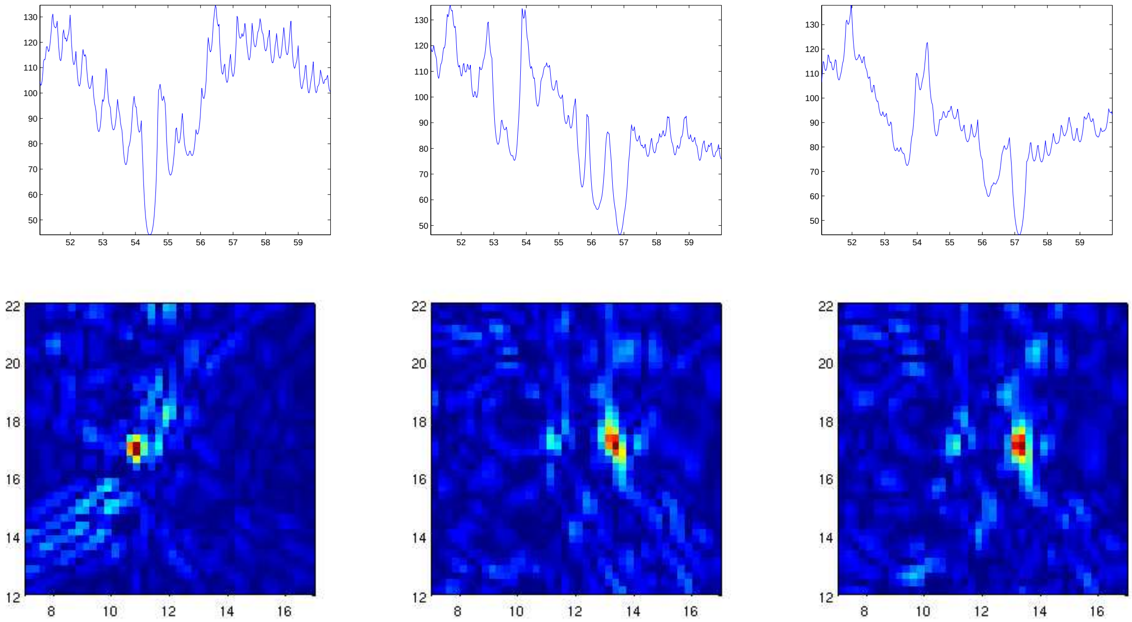

FIG. 14: BV norm versus time of the back propagated field in a square domain of size 10λ centered at $(12, 17)$ and snapshot of the back propagated field at time where BV norm is minimum. The damage is the cross presented on Fig. 11 . Each figure corresponds to a different illumination of the structure. ¿From left to right, illumination with sensor # 2, # 6 and # 10.

Cumulative images

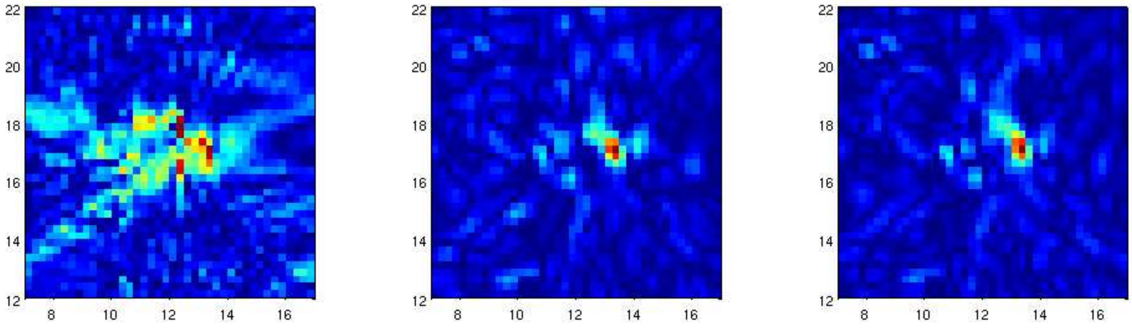

Cumulative images after thresholding

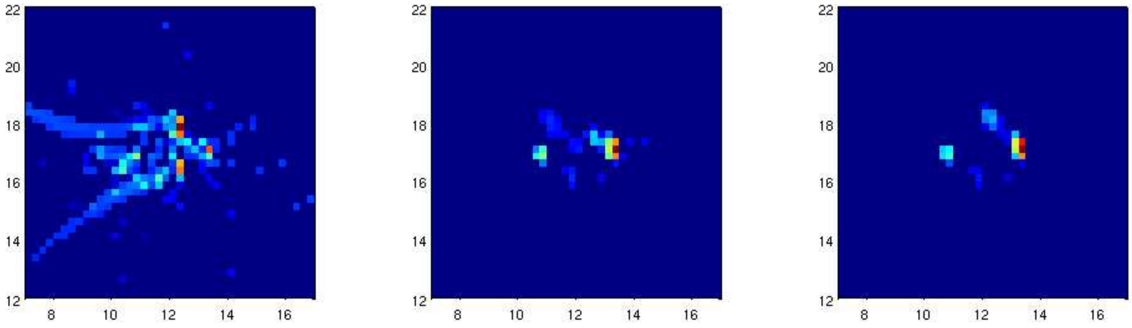

FIG. 15: Imaging of a the cross shaped defect depicted in Fig. 11. **Left:** Kirchhoff-Migration, **Middle:** Time-reversal imaging with entropy stopping, **Right:** Time-reversal imaging with BV stopping, **Top:** Cumulative images obtained by summation over each illumination as in Eq. (9). **Bottom:** Cumulative images after thresholding as discussed in Eq. (10).